Highlights

Can spinodal decomposition occur during decompression-induced vesiculation of magma?

Mizuki Nishiwaki

- Magma vesiculation during decompression was interpreted by simple thermodynamics.
- Binodal and spinodal curves of silicate–water systems were drawn versus pressure.
- Continuous decompression $\gtrsim$ several tens of MPa/s needed for spinodal decomposition.
- Magma vesiculation probably occurs by nucleation, not by spinodal decomposition.

Can spinodal decomposition occur during decompression-induced vesiculation of magma?

Mizuki Nishiwaki[a]

[a] *Center for Glass Science & Technology, School of Engineering, The University of Shiga Prefecture, 2500, Hassaka-cho, Hikone, Shiga, 522-8533, Japan*

Abstract

Volcanic eruptions are driven by decompression-induced vesiculation of supersaturated volatiles in magma. The initial phase has long been described as a process of nucleation and growth. Recently, it was proposed that spinodal decomposition—an energetically spontaneous phase separation that does not require a distinct interface—may occur during decompression. This idea has attracted attention, but support for it is currently limited to textural observations of experimental products, such as bubble number density independent of decompression rate and bubbles that are uniform in size and homogeneously distributed. In this study, hydrous magma was modeled as a two-component symmetric regular solution of silicate and water, allowing the spinodal curve to be determined from water solubility data coinciding with the binodal curve. In the low-pressure region from the magma chamber to the surface ($\lesssim$ 300 MPa), the spinodal curve lies at very low pressures ($\lesssim$ 10 MPa), and all previous laboratory decompression experiments were conducted within the nucleation region. Decompression paths, governed by the competition between decompression and water diffusion in the melt, indicate that spinodal decomposition without nucleation would require continuously very high decompression rates (tens of MPa/s), which are unlikely in natural systems where rates increase nonlinearly from deep to shallow regions. Although this simple model cannot fully capture the complexity of natural systems, the energetic framework provided by equilibrium thermodynamics remains a valid and insightful perspective for understanding magma vesiculation.

Keywords: hydrous magma, vesiculation, nucleation, spinodal decomposition, thermodynamics, regular solution

Table 1: Notation list.

Symbol	Unit	Definition
c	no unit	Water solubility in the melt (mole fraction)
g^{excess}	J mol^{-1}	Molar excess Gibbs energy for a regular solution
g^{ideal}	J mol^{-1}	Molar Gibbs energy for an ideal solution
g^{real}	J mol^{-1}	Molar Gibbs energy of mixing ($= g^{\mathrm{ideal}} + g^{\mathrm{excess}}$)
h^{excess}	J mol^{-1}	Molar excess enthalpy for a non-ideal solution
P	Pa	Pressure
P_{bi}	Pa	Pressure on the binodal curve (= binodal pressure)
P_{spi}	Pa	Pressure on the spinodal curve (= spinodal pressure)
R	J K^{-1} mol^{-1}	Gas constant
s^{excess}	J K^{-1} mol^{-1}	Molar excess entropy for a non-ideal solution ($= 0$ for a regular solution)
T	K	Temperature
w_{sym}	J mol^{-1}	Interaction parameter between two components for a symmetirc regular solution
$w_{\mathrm{A,\,B}}$	J mol^{-1}	Interaction parameter between two components for an asymmetric regular solution (Appendix A.1)
w_{ijk}	J mol^{-1}	Interaction parameter between three components for an asymmetirc regular solution (Appendix A.2)
X	no unit	Symbolic notation for chemical composition
x	no unit	Mole fraction of one of the two components
$x_{\mathrm{bi}}(P)$	no unit	The x that constitutes the binodal curve at pressure P
$x_{\mathrm{spi}}(P)$	no unit	The x that constitutes the spinodal curve at pressure P
τ_{dec}	s	Timescale of decompression
τ_{diff}	s	Timescale of water diffusion in the melt

1. Introduction

Magma degassing is a key controlling factor in the dynamics of volcanic eruptions. Volatiles (e.g., H_2O, CO_2, H_2S) initially dissolved in magma deep underground become insoluble during decompression, exsolving as vapor bubbles. Understanding this magma vesiculation process is crucial because it strongly influences eruption style and volcanic explosivity, playing

a key role in determining the time evolution of eruptions, ranging from effusive lava flows to highly explosive pyroclastic events. In particular, water often constitutes a large proportion of the volatile components, and its degassing—as phase separation into silicate melt saturated with water and supercritical water vapor saturated with trace silicate—has been extensively studied since Verhoogen (1951).

The initial degassing stage has long been understood as nucleation and growth (e.g., Sparks, 1978), and theoretical numerical models were constructed by Toramaru (1989, 1995) to predict the bubble number density (BND) based on classical nucleation theory (CNT, e.g., Hirth et al., 1970). In addition, over the past 30 years since the pioneering work by Hurwitz and Navon (1994), many laboratory experiments have been conducted to reproduce decompression-induced vesiculation of mainly hydrous magmas using magma analogues under controlled decompression rates. As data from decompression experiments to date generally agreed with numerical predictions (BND $\propto$ (decompression rate)$^{1.5}$ by Toramaru, 1995) based on CNT, Toramaru (2006) developed the BND decompression rate meter. This equation is valid for both homogeneous nucleation of spherical bubbles in a uniform melt (with large surface tension) and heterogeneous nucleation on crystal surfaces such as Fe–Ti oxides (with small surface tension), after applying appropriate corrections to the surface tension between the melt and bubble nuclei (Shea, 2017; Toramaru, 2022). This theoretical model has been widely used to estimate magma decompression rates in volcanic conduits through quantitative analysis of bubble textures in natural pyroclastic products (e.g., Giachetti et al., 2010; Houghton et al., 2010; Suhendro et al., 2022).

However, some laboratory experiments performed thus far have reported results that contradict the above equations; Allabar and Nowak (2018) performed decompression experiments on hydrous phonolitic melts over a wide range of decompression rates, including 0.024–1.7 MPa/s, and found consistently high BND values (5.2 mm^{-3}) independent of the decompression rate. To explain this result, they proposed a scenario in which spinodal decomposition, rather than nucleation as assumed in previous explanations, occurs in the early stages of decompression-induced vesiculation. Spinodal decomposition is the phase separation of a multi-component mixture or solid solution due to energetic instability (e.g., Cahn and Hilliard, 1959; Cahn, 1965). When the system's temperature, pressure, and chemical composition (T, P, X) are within the miscibility gap, whether nucleation

or spinodal decomposition occurs is determined by the sign of the second derivative of the system's molar Gibbs energy of mixing, g^{real}. If the sign is positive, the system is metastable, and nucleation occurs, with distinct phase boundaries (interfaces) appearing spatially random from the beginning. Conversely, if the sign is negative, the system becomes unstable, and spinodal decomposition occurs, in which initially small concentration fluctuations with an unclear phase boundary gradually grow and eventually lead to the separation of two phases at a specific wavelength, forming a distinct interface. The size distribution of the generated bubbles tends to be broader in the case of nucleation, whereas it becomes narrower in the case of spinodal decomposition. The diffusion coefficient is proportional to the second derivative of g^{real}, so nucleation corresponds to downhill diffusion, where diffusion progresses in the direction that weakens the concentration gradient. In contrast, spinodal decomposition corresponds to uphill diffusion, where diffusion progresses in the direction that strengthens the concentration gradient (Haasen, 1996).

In Allabar and Nowak (2018), spinodal decomposition was proposed for two reasons: (1) the timescale of spinodal decomposition in gas–liquid systems is much shorter than that of decompression (Debenedetti, 2000), which could explain the absence of dependence of BND on the decompression rate; and (2) the bubbles in the experimental products were nearly uniform in size, with a homogeneous spatial distribution; the vitrified silicate melt and bubbles appeared to have phase-separated at a specific wavelength. These findings were later supported by similar results obtained from experiments using the same phonolitic melt composition conducted by Allabar et al. (2020a, 2020b) and Marks and Nowak (2025a, 2025b). Building on this, Sahagian and Carley (2020) raised the problem that "the surface tension between the melt and tiny bubble nuclei should act to push exsolved volatiles back into the melt, yet bubbles of such small size form," and discussed this process as the "tiny bubble paradox." They extended the ideas of Allabar and Nowak (2018) by suggesting that if spinodal decomposition—rather than nucleation—occurs, this paradox can be resolved, since interface formation is no longer required. This interpretation explains the homogeneous spatial distribution of bubbles observed in some laboratory products. Thus, the new theory that "decompression-induced vesiculation of magma can occur not only through nucleation but also via spinodal decomposition" has been actively discussed and has attracted much attention over the last seven years. The review article on this topic by Gardner et al. (2023) also stated

that future interpretations of BND and bubble size distributions in natural volcanic products must consider the possibility that various mechanisms of bubble formation may occur, including nucleation (both homogeneous and heterogeneous) and spinodal decomposition.

However, whether spinodal decomposition actually occurs during decompression-induced magma vesiculation remains speculative. Nonetheless, owing to the small spatiotemporal scale of the physical phenomena under investigation, it is likely to be extremely difficult to confirm via laboratory observational experiments. Furthermore, magma vesiculation is a nonequilibrium process driven by supersaturation pressure. Previous studies have examined it in terms of the competition between decompression, which increases supersaturation, and water diffusion in the melt, which reduces it, quantified by the ratio of their respective timescales (e.g., Toramaru, 1995; Hajimirza et al., 2019; Marks and Nowak, 2025b). While such kinetic considerations are undoubtedly important, the fundamental criterion governing whether nucleation or spinodal decomposition occurs under given (T, P, X) conditions is the energetics derived from equilibrium thermodynamics, as outlined above. Determining which process predominates in natural systems, and the rate at which it proceeds, should therefore be addressed based on such equilibrium thermodynamic considerations.

This study first reviews the thermodynamic definitions of nucleation and spinodal decomposition. Spinodal decomposition, which has traditionally been discussed in the context of temperature changes at constant pressure, can also be described in terms of pressure changes at constant temperature. Here, hydrous magmas are simplified and modeled as a symmetric regular solution of silicate and water, and binodal and spinodal curves were quantitatively calculated on the chemical composition–pressure plane using the simple model. Based on these equilibrium thermodynamic calculations, I determined the boundary between nucleation and spinodal decomposition over a wide pressure range from the ground surface to near the second critical point. Furthermore, building on this, I considered, from a kinetic perspective, focusing on the competition between decompression and diffusion, which of the two processes—nucleation or spinodal decomposition—is more likely to occur in laboratory decompression experiments and natural systems, as well as the conditions under which they occur.

2. Thermodynamic energetics on the mixing of silicate and water

2.1. General theory

2.1.1. Two-component symmetric regular solution

Notations used in this study are listed in Table 1. Here, I explain the thermodynamics of a two-component mixture. In general, the molar Gibbs energy of a mixture, g^{real}, is expressed as the sum of the ideal solution's Gibbs energy, g^{ideal} (which arises from configurational entropy), and the excess energy, g^{excess} ($\neq 0$, represents the deviation from the ideal solution) (e.g., Guggenheim, 1952):

$$g^{\mathrm{real}} = g^{\mathrm{ideal}} + g^{\mathrm{excess}}, \tag{1}$$

where the Gibbs energies of the pure phases are proportionally combined and subtracted as the baseline. In an ideal solution, $g^{\mathrm{excess}} = 0$. Several types of non-ideal solutions take into account this deviation from the ideal solution, $g^{\mathrm{excess}} \neq 0$, among them the most basic type is the regular solution. In a regular solution, the non-ideal entropy is neglected ($s^{\mathrm{excess}} = 0$), and the non-ideal enthalpy is treated as $h^{\mathrm{excess}} \neq 0$, which leads to the relationship $g^{\mathrm{excess}} = h^{\mathrm{excess}}$. Let x be the mole fraction of one of the components ($0 < x < 1$). As explained below, g^{ideal} is always symmetric with respect to $x = 0.5$. The g^{ideal} at a given temperature T is given by:

$$g^{\mathrm{ideal}} = RT\{x \ln x + (1-x)\ln(1-x)\}. \tag{2}$$

On the other hand, the shape and expression of g^{excess} vary depending on whether a symmetric or an asymmetric model is adopted. In the case of the symmetric model,

$$g^{\mathrm{excess}} = x(1-x)w_{\mathrm{sym}}, \tag{3}$$

where w_{sym} is the interaction parameter between the two components A and B, representing the non-ideality of mixing. Fig. 1 shows a schematic diagram illustrating the energetics described above for a two-component symmetric regular solution.

In this study, as described later in Section 2.2, I approximate hydrous silicate melt as a two-component symmetric regular solution consisting of silicate and water. I also consider the possibility of approximating the system as an asymmetric regular solution (see Appendix A.1 for a two-component model and Appendix A.2 for a three-component model). However, I conclude

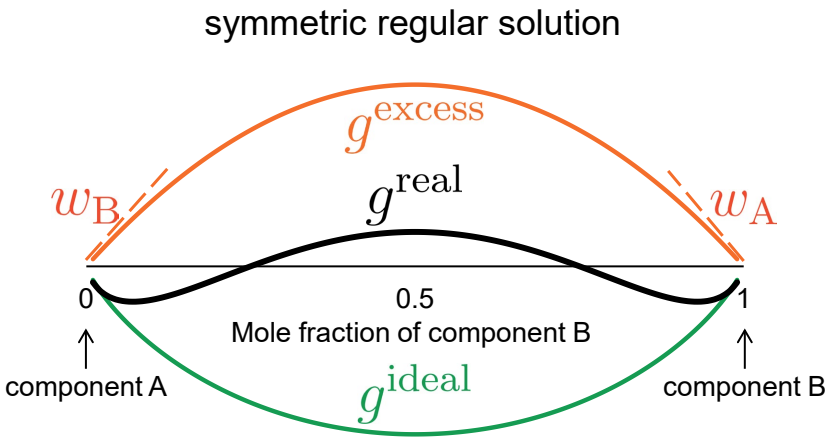

Figure 1: A schematic diagram of the molar Gibbs energy for a symmetric regular solution of two components, A and B. The green curve represents the molar Gibbs energy for an ideal solution, g^{ideal}, which is common to every regular solution model, including the asymmetric models described in Appendix A. The orange curve represents the molar excess Gibbs energy for a regular solution, g^{excess}, with symmetric and asymmetric models distinguished by the shape of this curve. The bold black curve represents the sum of these: the molar Gibbs energy of mixing, g^{real}. The interaction parameters w_{A} and w_{B} correspond to the slopes of the g^{excess} curve at the endpoints on the B and A side, respectively. In the symmetric model, $w_{\mathrm{A}} = w_{\mathrm{B}}$, which is denoted as w_{sym} in the text.

that a detailed investigation based on such models is currently impractical due to their mathematical complexity. Therefore, the application of models more complex than the symmetric model is beyond the scope of this study.

2.1.2. Binodal and spinodal curves

The g^{real} curve for the symmetric model and its corresponding phase diagram are shown in Fig. 2. Hereafter, we focus on conditions under which the system's temperature, pressure, and chemical composition (T, P, X) lie within the miscibility gap. Compositions outside the two local minima of the g^{real} curve correspond to a single-phase system, while compositions inside these minima undergo phase separation into a two-phase system. In other words, the points where the first derivative of the g^{real} curve with respect to x equals zero corresponds to the one-phase/two-phase boundary in the phase diagram (i.e., the binodal curve). In the region between the local minimum and the inflection point, where the g^{real} curve is convex downward (i.e., where the second-order derivative with respect to x is positive), the system is metastable, and nucleation occurs with distinct phase boundaries

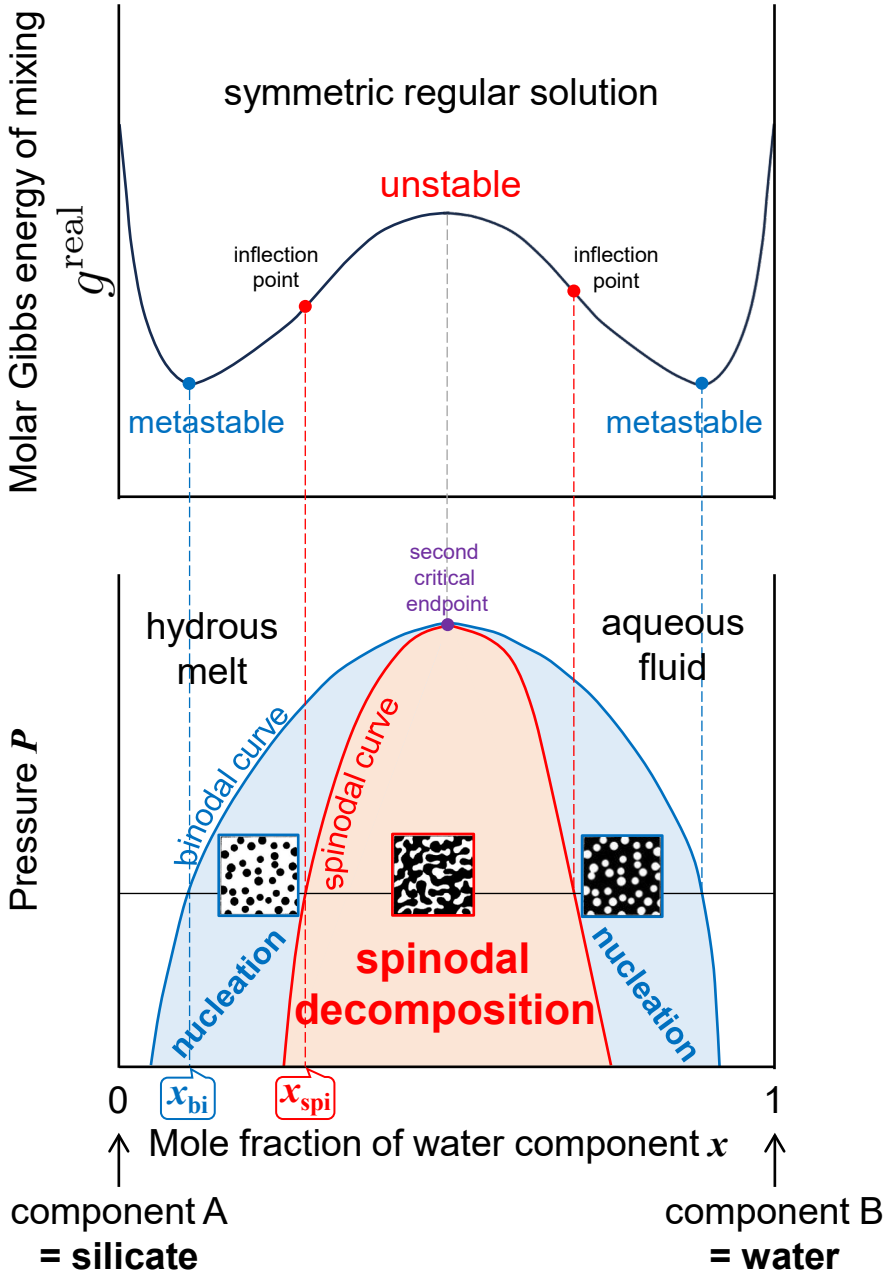

Figure 2: Schematic molar Gibbs energy of mixing, g^{real} (upper panel), and the corresponding phase diagram (lower panel) for a general two-component symmetric regular solution. In the interval where the g^{real} curve is convex downward, the system is metastable, and nucleation occurs with clear phase boundaries (surfaces) appearing randomly in space. On the other hand, when the g^{real} curve is convex upward, the system is unstable, and spinodal decomposition occurs, wherein the two phases start to separate at a specific wavelength with indistinct phase boundaries.

(interfaces) appearing randomly in space. Conversely, in the interval where the g^{real} curve is convex upward (i.e., where the second derivative with respect to x is negative), the system is unstable, and spinodal decomposition occurs, wherein the two phases start to separate at a specific wavelength with indistinct phase boundaries. In other words, the points where the second derivative of the g^{real} curve with respect to x equals 0 correspond to the nucleation/spinodal decomposition boundary (i.e., the spinodal curve) in the phase diagram. Mathematically,

$$\left(\frac{\partial g^{\mathrm{real}}}{\partial x}\right)_{T,P} = RT \ln\left(\frac{x}{1-x}\right) + (1-2x)w_{\mathrm{sym}}, \tag{4}$$

$$\left(\frac{\partial^2 g^{\mathrm{real}}}{\partial x^2}\right)_{T,P} = \frac{RT}{x(1-x)} - 2w_{\mathrm{sym}}, \tag{5}$$

the solutions x when these equations are equal zero form the binodal and spinodal curves, respectively. From here on, each x will be referred to as x_{bi} and x_{spi}, respectively. Binodal and spinodal curves appear on the cross-sections of binodal and spinodal surfaces in temperature–pressure–chemical composition space (e.g., Aursand et al., 2017). Hence, either temperature or pressure can be selected for the vertical axis in the lower panel of Fig. 2. This will be explained in Section 2.4. Combining Eqs. (4) and (5) and eliminating w_{sym}, the following relation between x_{bi} and x_{spi} is derived:

$$x_{\mathrm{spi}} = \frac{1}{2}\left\{1 - \sqrt{1 - \frac{2(1-2x_{\mathrm{bi}})}{\ln\dfrac{1-x_{\mathrm{bi}}}{x_{\mathrm{bi}}}}}\right\}. \tag{6}$$

This relation is shown in Fig. 3 for the range $0 < x < 0.5$, corresponding to the left half area of Fig. 2. This range is focused on to utilize knowledge about the silicate-rich side (e.g., the solubility of water in magma). The relation $x_{\mathrm{spi}} > x_{\mathrm{bi}}$ holds for all values in the range.

2.2. Treatment of hydrous magma

It is well known that silicate melts, which are mixtures of multiple oxides, can separate into several distinct phases in response to changes in temperature and pressure, both in natural and industrial compositions: for

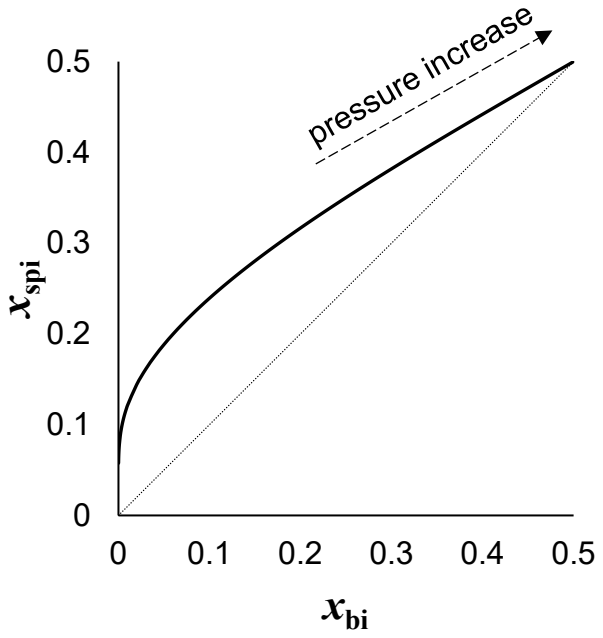

Figure 3: The relationship between x_{bi} and x_{spi} for the two-component symmetric regular solution model at an arbitrary fixed temperature, derived from Eqs. (4) and (5), which represent the first- and second-order derivatives of g^{real} with respect to x. x_{bi} and x_{spi} are the values of x that constitute the binodal and spinodal curves, respectively. Increases in x_{bi} and x_{spi} correspond to increasing pressure. The range $0 < x < 0.5$ corresponds to the left half of Fig. 2. The relation $x_{\mathrm{spi}} > x_{\mathrm{bi}}$ holds throughout the entire range.

example, liquid–liquid separation as reported by Roedder (1978), Charlier and Grove (2012), and Thivet et al. (2023). Dehydration of magma is no exception and can be viewed as separation into a liquid phase (water-saturated silicate melt) and a vapor phase (silicate-saturated water vapor), i.e., liquid–vapor separation. In this study, hydrous magma is approximated as a regular solution consisting of two components: anhydrous silicate (melt) and water (vapor), and the thermodynamics of mixing these two components is considered. Therefore, in the following, components A and B represent silicate and water, respectively.

It is important to note that, in reality, water in magma exists as two molecular species: molecular water H_2O_m and hydroxyl groups $-OH$ (e.g., Stolper, 1982a; 1982b). The mechanisms by which these two species dissolve into and exsolve from silicate melts are entirely different, and their speciation varies with temperature and pressure. This difference may significantly affect whether hydrous melt can be regarded as a symmetric regular solution. To properly account for this effect and quantitatively discuss the asymmetry, it is necessary to treat H_2O_m and $-OH$ as distinct components and formulate the Gibbs energy of mixing in a ternary system that includes the bridging oxygen in the anhydrous silicate (Nishiwaki, 2023). However, this approach is still in a trial-and-error stage and remains highly challenging. Therefore, a detailed discussion is deferred to Appendix A.2. For this reason, these species are considered together here; that is, x is the mole fraction of total water.

Additionally, at and near the silicate end member, a crystalline phase precipitates at low temperatures (e.g., Fig. 7 in Paillat et al., 1992; and Fig. 3 in Makhluf et al., 2020 for the albite–H_2O system). However, in this study, it is neglected, assuming the amount to be minute and the system to be at a sufficiently high temperature for this assumption to hold, for simplicity.

2.3. Consistency with known phase diagrams

Next, we evaluate the validity of the two-component symmetric regular solution approximation by comparing it with established phase diagrams. In Fig. 2, the regions on the silicate-rich and water-rich sides at pressures higher than the binodal curve correspond to hydrous melt and aqueous fluid, respectively. Thus, when a pressure change occurs that crosses the binodal curve at a fixed chemical composition, the reaction "magma (supercritical fluid) $\leftrightarrow$ water-saturated silicate melt (hydrous melt) + nearly pure water vapor (aqueous fluid)" occurs. The rightward reaction indicates

exsolution with decompression, whereas the leftward reaction indicates mutual dissolution with compression. For example, according to the results of high-temperature and high-pressure experiments shown in Fig. 3 of Makhluf et al. (2020), for the albite–water system at 900°C, the second critical endpoint (the vertex of the miscibility gap) is in the range of 1.25–1.40 GPa and 42–45 wt%, i.e., $x = 0.57$–0.60 (on a single oxygen basis). While some experimental studies have indicated that the position of the second critical endpoint may vary depending on temperature and the chemical composition of silicate (Bureau and Keppler, 1999; Sowerby and Keppler, 2002), in this study, I assume that it does not deviate significantly from $x = 0.5$ to justify the use of the symmetric regular solution approximation, as mentioned in the previous section. This assumption may be somewhat bold, but it is the simplest model currently available and serves as a baseline for comparison when the detailed shape of the Gibbs energy is determined in the future and the model is updated.

2.4. Spinodal decomposition with pressure change

Spinodal decomposition is a phenomenon originally discovered in the field of inorganic materials such as ceramics and alloys (e.g., Cahn, 1965), and is typically discussed in terms of phase separation into solid–solid, solid–liquid, or liquid–liquid systems that occur with decreasing temperature at ambient pressure. Thus, temperature is typically used as the vertical axis when drawing phase diagrams. In contrast, when considering whether spinodal decomposition occurs during phase separation of magma into gas–liquid systems, I assumed constant temperature and focused on phase separation occurring during decompression, since water solubility is much more dependent on pressure than temperature (e.g., Yamashita, 1999; Liu et al., 2005). Therefore, pressure was adopted as the vertical axis in the phase diagram shown in Fig. 2.

It has been suggested that, in nature, magma degassing may be more efficiently driven by heating caused by latent heat of crystallization, viscosity, and friction rather than decompression (e.g., Lavalée et al., 2015). However, decompression experiments are typically conducted at constant temperature, and so far, scenarios of spinodal decomposition have been proposed based solely on the results of such experiments (Allabar and Nowak, 2018; Allabar et al., 2020b; Sahagian and Carley, 2020; Gardner et al., 2023; Marks and Nowak, 2025a; 2025b). Therefore, focusing on the pressure axis to test the validity of this scenario is not necessarily an unreasonable assumption.

3. Calculation methods

3.1. Relation between the water solubility curve and the binodal curve, and calculation of the spinodal curve

The section for $x < 0.5$ of the binodal curve on the x–P plane at constant T, shown in the lower panel of Fig. 2, should coincide with the solubility curve of water in the silicate melt at that temperature with respect to pressure change. In other words, the water solubility $c(P)$ in the silicate melt is equal to $x_{\mathrm{bi}}(P)$, which constitutes the binodal curve. From this and the relation given by Eq. (6) between x_{bi} and x_{spi}, it is possible to calculate the value of x_{spi} that constitutes the spinodal curve. The value of the silicate–water interaction parameter $w_{\mathrm{sym}}(P)$ at a fixed temperature can also be determined by substituting the value of $x_{\mathrm{bi}}(P)$ into Eq. (4) or the value of $x_{\mathrm{spi}}(P)$ into Eq. (5).

3.2. Conditions on the temperature, chemical composition, and water solubility in magma

Three types of silicate melts are assumed for temperature and chemical composition: K-phonolitic melt at 1,050°C, basaltic melt at 1,100°C, and albite melt at 900°C. The conditions for the phonolitic melt are the same as those used in all experiments by Allabar and Nowak (2018). Basaltic and albite melts were chosen to compare and examine the behavior of the spinodals at higher pressures. The temperatures employed correspond to those at which the pressure dependence of water solubility in the melt has already been systematically determined by high-temperature and high-pressure experiments. According to Iacono-Marziano et al. (2007), who performed decompression experiments using AD79 Vesuvius pumice similarly to Allabar and Nowak (2018), the water solubility in K-rich phonolitic melt at 1,050°C agrees well with values calculated from the empirical model of Moore et al. (1998). Their formula was therefore also used in this study for the pressure range 0.1–300 MPa. Note that Moore et al. (1998) defined the mole fraction of water by treating each oxide (e.g., SiO_2 and Al_2O_3) as one unit. However, this definition is no longer commonly used, and here, the mole fraction was converted to the currently common single-oxygen basis values (see Section 1.2 in Zhang, 1999). The water solubility in the basaltic melt at 1,100°C was obtained by digitizing the fitting curve of experimentally determined values for $\lesssim$ 600 MPa, as shown in Fig. 2 of Hamilton et al. (1964). The water solubility in the albite melt at 900°C was also obtained

by digitizing the fitting curve of the experimentally determined values for $\lesssim 1000$ MPa, as shown in Fig. 8 of Burnham and Jahns (1962).

4. Calculation results

The binodal and spinodal curves drawn on the x–P plane for the three silicate–water systems are shown in Fig. 4. The geometric characteristics of both curves are similar regardless of the silicate composition. Fig. 6 in Allabar and Nowak (2018) and Fig. 1 in Sahagian and Carley (2020) show conceptual phase diagrams in which both the binodal and spinodal curves are convex upward over the entire chemical composition range, with a large area inside the spinodal curve. The lower panel of Fig. 2 in this study is consistent with this. However, when considering their actual positions and shapes quantitatively based on chemical thermodynamics, the solubility curve (= binodal curve) is convex downward at $\lesssim 400$ MPa (approximately following the relation $c(P) \propto P^{0.5}$); therefore, the spinodal curve is also convex downward. In the pressure range examined in this study, the spinodal curve is situated at a much lower pressure relative to the binodal curve at a given water content. For example, at $x = 0.10$, the water solubility (wt%), P_{bi} (MPa), and P_{spi} (MPa) for the phonolitic melt, basaltic melt, and albite melt are (5.4, 219, < 1), (5.2, 239, 6), and (5.8, 166, 10), respectively. Furthermore, as x increases, the corresponding P_{spi} gradually shifts toward higher pressures, but the difference from P_{bi} remains very large. In other words, the nucleation region is much broader than the spinodal decomposition region, at least in the range $x < 0.25$ plotted in Fig. 4. For example, in the case of albite melt, $P_{\mathrm{bi}} = 1000$ MPa corresponds approximately to $P_{\mathrm{spi}} = 190$ MPa.

The calculation results for $w(P)$ are shown in Fig. 5. Although w is large at 0.1 MPa (phonolite: 75 kJ/mol, basalt: 85 kJ/mol, and albite: 95 kJ/mol), it monotonically decreases rapidly with increasing pressure over the entire pressure range for all three chemical compositions. This behavior is consistent with the fact that mutual dissolution of silicate and water proceeds more extensively at higher pressures at a fixed temperature, thereby narrowing the miscibility gap.

5. Discussion

In decompression-induced vesiculation of magma, the pressure and chemical composition (water content) at which the boundary between

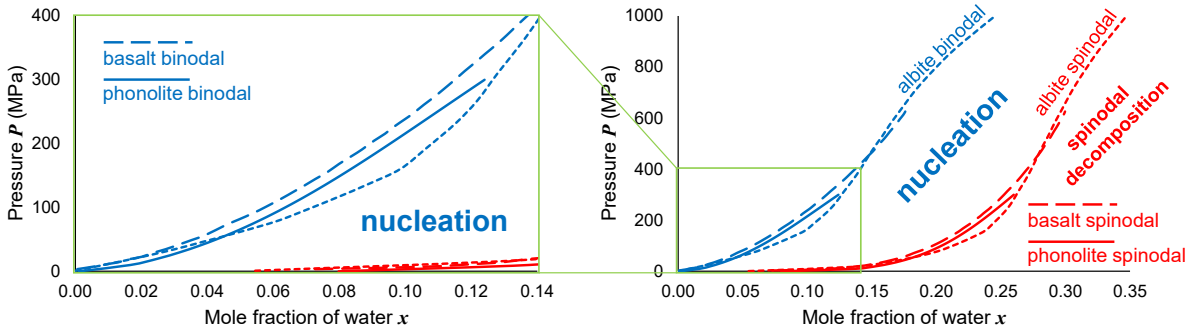

Figure 4: Binodal (blue) and spinodal (red) curves for hydrous melts of 1,050°C K-phonolitic (solid line), 1,100°C basaltic (dashed line), and 900°C albite (dotted line) compositions in the pressure range 0.1–1000 MPa. The left panel shows an enlargement of the right panel, focusing on pressures below 400 MPa. The binodal curves correspond to the water solubility curves in the melt for each chemical composition (Moore et al., 1998; Hamilton et al., 1964; Burnham and Jahns, 1962). The positions of spinodal curves were determined based on the positions of binodal curves and Eq. (6).

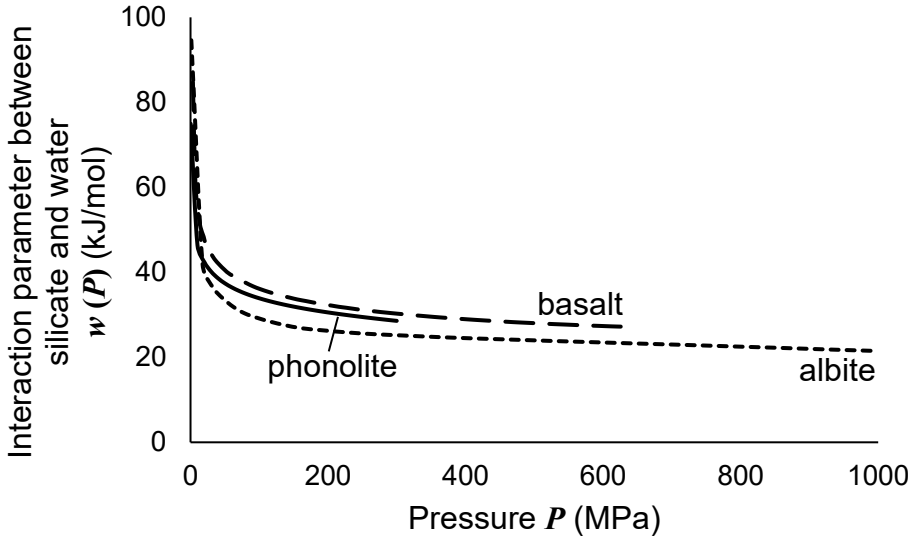

Figure 5: Calculation results of the interaction parameter between silicate and water, $w(P)$, for hydrous K-phonolitic melt at 1,050°C over 0.1–300 MPa (solid line), basaltic melt at 1,100°C over 0.1–625 MPa (dashed line), and albite melt at 900°C over 0.1–1000 MPa (dotted line).

nucleation and spinodal decomposition occurs are determined by energetic considerations based on equilibrium thermodynamics, as discussed in the preceding sections. However, since these phase separation processes proceed under non-equilibrium conditions, assessing which process dominates in natural systems, as well as their rates of progression, requires consideration of kinetic effects. In this section, I define the lower pressures as $\lesssim$ 300 MPa, which encompasses the typical pressure range relevant to volcanic eruption dynamics (from the magma reservoir to the ground surface) and is well represented by decompression experimental data. The higher pressure range is defined as $\gtrsim$ 1 GPa, near the second critical point where silicate melt and aqueous fluid behave as a single phase. I examine phase separation in each of these pressure regions from both thermodynamic equilibrium and kinetic perspectives.

5.1. At lower pressures

5.1.1. Thermodynamic equilibrium perspective

All nucleation pressure values from 88 previous experimental runs from Gardner et al. (1999) to Le Gall and Pichavant (2016), compiled and calculated by Shea (2017), fall within the nucleation region shown in Fig. 4, assuming variations in melt chemical composition are disregarded. Additionally, almost all recent experimental runs using 1,050°C phonolitic melt were conducted from an initial pressure of 200 MPa down to a final pressure of 20-–110 MPa, or from 270 MPa down to 100-–150 MPa (Allabar and Nowak, 2018; Allabar et al., 2020b; Marks and Nowak, 2025a; 2025b). Since these final pressures are higher than P_{spi}, the nucleation pressures of these runs inevitably lie within the nucleation region. Therefore, the innovative scenario proposed by Allabar and Nowak (2018) and Sahagian and Carley (2020)—that spinodal decomposition occurs during magma decompression—is not an adequate explanation for the experimental results showing high BND values that are independent of decompression rate.

5.1.2. Kinetic perspective

Next, I discuss the possibility of spinodal decomposition in decompressing magma from the perspective of the decompression path depicted on the phase diagram. Given that $P_{\mathrm{spi}} \ll P_{\mathrm{bi}}$ and the spinodal region is extremely narrow, as shown in the quantitatively plotted left panel of Fig. 4, a new schematic diagram (Fig. 6) is introduced. Consider a melt that is initially undersaturated or just saturated with water. Upon the initiation

of decompression, the melt pressure passes through the saturation pressure (i.e., binodal pressure). From this point onward, a competition arises between the accumulation of supersaturation pressure due to decompression and its relaxation via diffusion of water molecules into the bubble nuclei. The balance between these processes determines how water exsolution from the melt proceeds—that is, the decompression path. This competition between diffusion and decompression can be evaluated by comparing their characteristic timescales (e.g., Toramaru, 1995) and has been widely applied in the interpretation of decompression experiment results (Hajimirza et al., 2019; Marks and Nowak, 2025b). The diffusion timescale is denoted as τ_{diff}, and the decompression timescale as τ_{dec}. The ratio $\tau_{\mathrm{diff}}/\tau_{\mathrm{dec}}$ is theoretically predicted to relate to BND as follows (Toramaru, 1995; 2006):

$$\mathrm{BND} \propto \left(\frac{\tau_{\mathrm{diff}}}{\tau_{\mathrm{dec}}}\right)^{1.5} \propto \left(\frac{\text{decompression rate}}{\text{water diffusivity}}\right)^{1.5}. \tag{7}$$

This concept has been applied to interpret the results of decompression experiments (Hajimirza et al., 2019; Marks and Nowak, 2025b). Hajimirza et al. (2019) conducted rapid decompression experiments on rhyolitic melt at 825–875°C, starting from initial pressures of 160–250 MPa and decompressing to a wide range of final pressures. The decompression rates were very high, ranging from 2.7 to 180.3 MPa/s, and the ratio $\tau_{\mathrm{diff}}/\tau_{\mathrm{dec}}$ covered a wide range from 1.3×10^{-1} to 8.1×10^{3} (see Table 3 in their paper). In contrast, Marks and Nowak (2025b) perfomed experiments with decompression rates of 0.064, 0.17, and 1.7 MPa/s, where the range of $\tau_{\mathrm{diff}}/\tau_{\mathrm{dec}}$ was relatively low, from 0.01 to 7.3 (see Table 1 in their paper).

Decompression-controlled regime. When diffusion is sufficiently faster than decompression (i.e., $\tau_{\mathrm{diff}} \ll \tau_{\mathrm{dec}}$: the decompression-controlled regime), the nucleation rate increases sharply with the rise in supersaturation pressure due to decompression, but subsequently decreases rapidly owing to diffusion-driven bubble growth. The BND exhibits an abrupt increase immediately before the nucleation peak and, once reaching its maximum, remains constant (Toramaru, 2025). The system then undergoes near-equilibrium degassing along the binodal curve (Fig. 6). This behavior has been demonstrated by numerical simulations (e.g., Toramaru, 1995; 2025) and decompression experiments (e.g., Mangan et al., 2004; Hajimirza et al., 2019). Similar to the runs by Hajimirza et al. (2019) and Marks and Nowak (2025b) with the same initial pressure of 200 MPa, which yielded

BND values of 10^{14}–10^{15} m^{-3}, this regime is characterized by very high BND. Marks and Nowak (2025b) claimed that this bubble population was produced by spinodal decomposition. However, as shown in Fig. 6, the equilibrium degassing path is far from the spinodal decomposition region, and the two are incompatible. Therefore, it is reasonable to conclude that this bubble population was formed by nucleation.

Diffusion-controlled regime. When decompression is sufficiently faster than diffusion (i.e., $\tau_{\mathrm{diff}} \gg \tau_{\mathrm{dec}}$; the diffusion-controlled regime), one might expect a further increase in BND. However, due to slow diffusion, the number of nucleated bubbles remains small, resulting in incomplete relaxation of the supersaturation pressure. Consequently, the nucleation rate either continues to increase or remains nearly constant, causing the BND to increase over time. This situation essentially corresponds to heterogeneous nucleation ("HEN Time-control" in Toramaru, 2025). In this case, the exponent in Eq. (7) decreases from 1.5 to 0 and eventually to –1 with increasing $\tau_{\mathrm{diff}}/\tau_{\mathrm{dec}}$. Indeed, Hajimirza et al. (2019) observed continuous "incomplete nucleation" persisting from the onset of nucleation at the final pressure until the end of the hold time. Furthermore, in Hajimirza et al. (2022) Suite 4 (initial pressure 200 MPa) with an extended hold time, the maximum BND reached was confirmed to be less than 10^{13} m^{-3}. In another study, Marks and Nowak (2025b) reported that BND decreased to less than 10^{8} m^{-3} due to bubble coalescence. This is likely attributable to the slower decompression rate, longer decompression time, or lower viscosity compared with Hajimirza's experiments. In other words, both experiments yielded smaller BND values than those in the decompression-controlled regime.

Extremely rapid decompression. For spinodal decomposition to occur without nucleation, it is necessary to maintain sufficient supersaturation pressure despite a large decompression from an initial pressure higher than P_{bi} to a pressure lower than P_{spi}. This condition requires the ratio $\tau_{\mathrm{diff}}/\tau_{\mathrm{dec}}$ to be very large; in other words, the decompression rate must be extremely high and the diffusivity very low. According to Table 3 of Hajimirza et al. (2019), Run G-1614 with a hold time of 0 s was decompressed from an initial saturation pressure of 160 MPa to 13.0 MPa at a rapid decompression rate of 15.5 MPa/s, yielding a high ratio $\tau_{\mathrm{diff}}/\tau_{\mathrm{dec}} = 2.3 \times 10^{3}$. Nevertheless, bubbles nucleated during decompression (BND $= 1.05 \times 10^{9}$ m^{-3}). Thus, an even faster decompression rate (at least several tens of MPa/s) to a

lower pressure (a few MPa) would be required. If such decompression were possible, the very large supersaturation pressure at the final pressure would be relaxed by spinodal decomposition, and in some cases might subsequently cross the binodal curve to trigger nucleation. Moreover, when such extremely rapid decompression is applied to high-viscosity melts, the diffusion timescale becomes negligible, and the competition between the timescales of viscosity and decompression may cause the BND to change abruptly, entering the viscosity-controlled regime (Nishiwaki and Toramaru, 2019).

In natural systems. As discussed above, reaching the spinodal decomposition region without bubble nucleation requires maintaining an extremely high decompression rate of at least several tens of MPa/s continuously from the magma reservoir to the ground surface. However, numerical simulations (e.g., Hajimirza et al., 2021) suggest that decompression during explosive Plinian eruptions proceeds nonlinearly, starting at around 0.1 MPa/s in deep magma storage regions and accelerating to approximately 10 MPa/s near the shallow conduit. Therefore, the likelihood of natural magma undergoing spinodal decomposition without prior nucleation is expected to be exceedingly low.

5.2. At higher pressures

5.2.1. Thermodynamic equilibrium perspective

On the other hand, in regions of higher pressure and higher water content, beyond the range shown in Fig. 4, P_{spi} asymptotically approaches P_{bi}, and spinodal decomposition becomes more likely. In other words, spinodal decomposition may occur if decompression passes near the apex of the second critical endpoint. Moreover, since the second critical endpoint of silicate–water systems has been reported to shift to lower temperatures and pressures with increasing amounts of alkali metal oxides (e.g., Na_2O and K_2O) in the silicate (Bureau and Keppler, 1999; Sowerby and Keppler, 2002), Allabar and Nowak (2018) suggested that spinodal decomposition at low pressures may be more likely in alkali-rich phonolitic melts than in other silicic silicates.

However, as long as the symmetric regular solution approximation is assumed, the shift of the second critical endpoint to lower pressures, i.e., the shift of the binodal curve to lower pressures, is accompanied by a corresponding shift of the spinodal curve, because x_{bi} and x_{spi} change in tandem, as shown in Fig. 3. In this case, the region of spinodal decomposition shown in Fig. 4 would become narrower, making spinodal decomposition

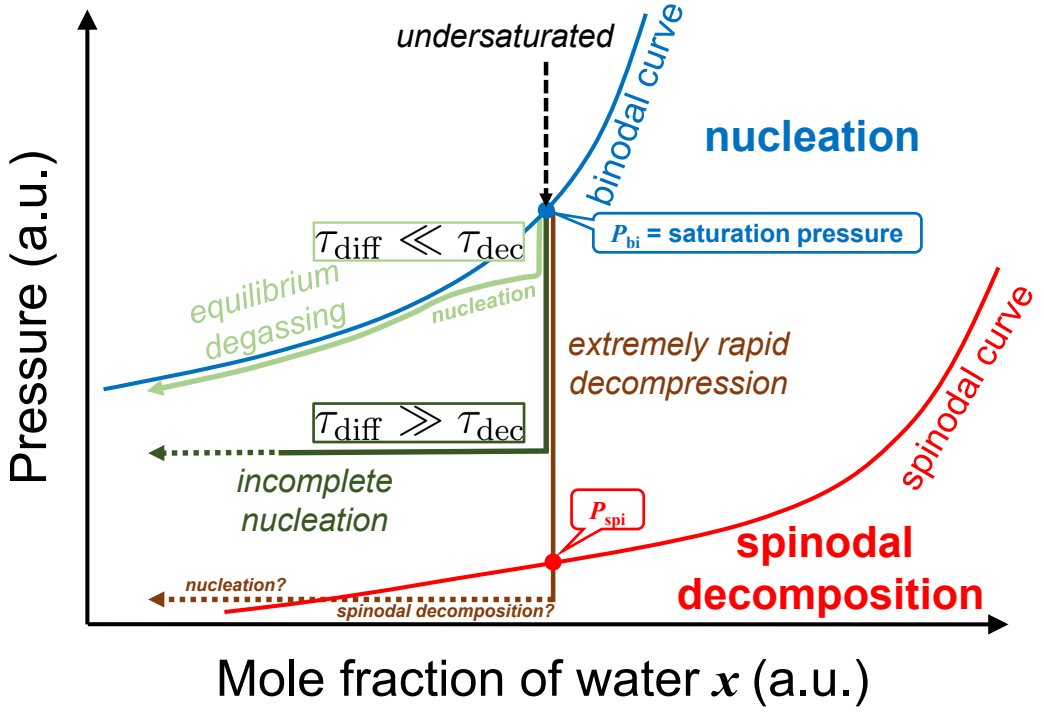

Figure 6: Schematic diagram showing decompression paths on the x–P plane. The positions of the binodal and spinodal curves are determined by equilibrium thermodynamics, whereas the decompression path is controlled by kinetic effects: the balance between the increase in supersaturation pressure due to decompression and its decrease due to diffusion of water molecules into the bubble nuclei. In the case of $\tau_{\rm diff} \ll \tau_{\rm dec}$ (the decompression-controlled regime, light green), rapid nucleation occurs only within a narrow pressure range, and the system with a fixed BND follows the binodal curve, resulting in equilibrium degassing with bubble growth only. In contrast, when $\tau_{\rm diff} \gg \tau_{\rm dec}$ (the diffusion-controlled regime, dark green), large supersaturation persists even at the final pressure, and BND increases monotonically over time at an almost constant nucleation rate, leading to incomplete nucleation as observed in Hajimirza et al. (2019). Furthermore, assuming an extreme case of $\tau_{\rm diff} \gg \tau_{\rm dec}$ (extremely rapid decompression, brown), if the pressure drops below the spinodal pressure $P_{\rm spi}$ before nucleation occurs, spinodal decomposition (possibly followed by nucleation) is expected to occur to relax the very large supersaturation pressure.

less likely. Therefore, if spinodal decomposition is more likely to occur in phonolitic melts, the binodal curve of the phonolite–water system is expected to be highly asymmetric, making the symmetric regular solution approximation inapplicable. This might be related to the effective ionic radius of potassium (1.38 Å), which is abundant in phonolitic melt and is as large as that of oxygen (1.40 Å) (Shannon, 1976). The packing ratio is thus higher than that in alkali-poor silicates (e.g., albite and rhyolite). Still, the shape of the binodal curve of the phonolite-–water system remains unknown, and additional complexities not accounted for in the symmetric model used in this study will likely require detailed high-temperature and high-pressure experiments to elucidate fully.

5.2.2. Kinetic perspective

Wang et al. (2021) performed in-situ observations of phase separation in peralkaline aluminosilicate ($Na_3AlSi_5O_{13}$)–water systems within a single-phase supercritical fluid near the second critical endpoint (approximately 700°C and 1 GPa) using a hydrothermal diamond anvil cell. They observed that at specific composition ratios (37–51 wt% aluminosilicate), a network structure of hydrous silicate melt emerged as temperature decreased, resulting in phase separation where aqueous fluid was enclosed within the silicate melt (i.e., spinodal decomposition). In addition, in situ Raman spectroscopy data revealed that polymerized aluminosilicate species tended to concentrate in the silicate melt, while silica monomers preferentially accumulated in the aqueous fluid. This phenomenon was interpreted by referring to the viscoelastic phase separation (VPS) theory for polymer solutions (Tanaka, 1994). The theory suggests that the relatively large silicate polymers and small water molecules differ significantly in relaxation timescales (viscoelastic properties), leading to phase separation in a network-like structure.

Their experimental results with a peralkaline composition offer a new perspective for interpreting the findings of Allabar and Nowak (2018); Allabar et al. (2020b); Marks and Nowak (2025a, 2025b), all of which involved alkali-rich phonolite. Contrary to the traditional view of spinodal decomposition (the so-called "intertwined structure" shown in Fig. 2), the observed network-like phase separation suggests that the inference made from phonolite experiments—that attributes the bubble spatial distribution, which appeared to follow a specific wavelength, to spinodal decomposition—may not be valid.

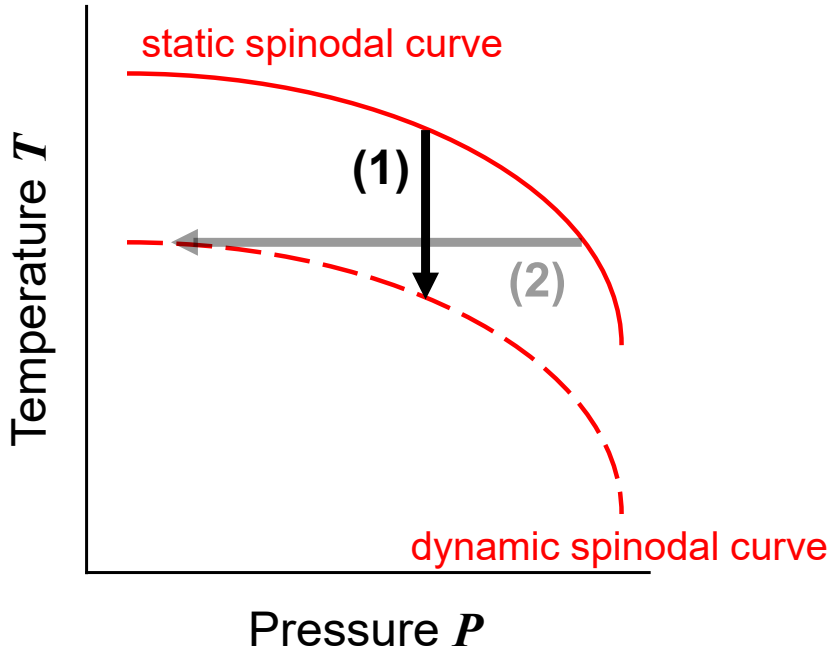

Figure 7: Schematic relationship between the static and dynamic spinodal curves on the P–T plane for a fixed composition. (1) At constant pressure, the dynamic spinodal curve shifts to the lower temperatures compared to the static one (Wang et al., 2021). (2) In this case, at a fixed temperature, the spinodal curve shifts to the lower pressures.

According to Wang et al. (2021), at constant pressure, the dynamic spinodal curve shifts to lower temperatures compared to the static one. This shift is illustrated by arrow (1) in Fig. 7, where the spinodal curve is drawn with a negative slope, assuming it is similar to the negative slope of the phase boundary (binodal curve) appearing in the P–T plane at fixed composition. In this case, at fixed temperature, the spinodal curve shifts toward lower pressures, as illustrated by arrow (2) in Fig. 7. In other words, if kinetic effects similar to those observed in their experiments were to occur in an isothermal decompression system, the dynamic spinodal curve would shift to pressures even lower than the static spinodal pressure P_{spi}. Furthermore, if this shift also occurred in the low-pressure region discussed in Section 5.1, spinodal decomposition would become even less likely.

6. Conclusions

In this study, hydrous magma was approximated as a two-component symmetric regular solution composed of silicate and water. Using the known solubility of water in magma, which coincides with the binodal curve, I determined the position of the spinodal curve on the chemical composition (water content)–pressure plane. As a result, it was found that in the low-pressure region extending roughly from the magma reservoir to the ground surface ($\lesssim$ 300 MPa), the spinodal curve is located at very low pressures, below about 10 MPa. All previous laboratory decompression experiments have been conducted within the pressure range between these two curves, that is, within the nucleation region.

Furthermore, decompression paths, determined by the competition between decompression and water diffusion in the melt affecting supersaturation pressure, were introduced on the phase diagram. By comparing the timescales of these two processes, cases were categorized. Comparing this with decompression experiments using rhyolitic melt showed that for spinodal decomposition to occur in decompressing magma without nucleation, a very large decompression rate of at least several tens of MPa/s must be sustained from the binodal curve (i.e., saturation pressure) down to below the spinodal pressure. However, recent numerical simulations suggest that in explosive Plinian eruptions, magma decompression rates nonlinearly increase from deep to shallow regions. From these considerations, it is concluded that the possibility of spinodal decomposition occurring in natural magma decompression systems is extremely low.

In contrast, in the high-pressure region ($\gtrsim$ 1 GPa), the spinodal curve asymptotically approaches the binodal curve as the second critical endpoint is approached, so spinodal decomposition is expected to be more likely than in the low-pressure region. However, previous in-situ observations have demonstrated that, because silicate polymers and water molecules differ greatly in their viscoelastic properties, phase separation by spinodal decomposition produces a network-like rather than an intertwined microstructure. Such kinetic effects could shift the actual dynamic spinodal curve to lower temperatures and pressures than its static counterpart determined from equilibrium thermodynamics, thereby further reducing the likelihood of spinodal decomposition even in the low-pressure region.

Although decompression-induced vesiculation of magma is an inherently non-equilibrium process, discussions of phase separation should first

be grounded in the energetic perspective provided by equilibrium thermodynamics. While this simple model cannot fully capture the complexity of natural systems, The model adopted in this study is a highly simplified and classical approach, yet it demonstrates that equilibrium thermodynamics can still offer a valid and insightful physical perspective even for contemporary debates in volcanology.

Appendix A. Assymetric regular solution models

In this study, hydrous magma is approximated as a regular solution composed of silicate and water. I examine whether a symmetric or an asymmetric form of the molar excess Gibbs energy is more appropriate. For the asymmetric form, two cases are considered: one in which molecular water (H_2O_m) and hydroxyl groups ($-OH$) are not distinguished (two-component system), and another in which they are distinguished (three-component system). Based on both observational and experimental evidence for the behavior of real systems, as well as the mathematical convenience of the models, the main text adopts a two-component symmetric model. For comparison, the two-component asymmetric model is described in Appendix A.1, and the three-component asymmetric model in Appendix A.2.

Appendix A.1. Two-component asymmetric model

In the case of a two-component asymmetric regular solution, the molar excess Gibbs energy g^{excess} is expressed as:

$$g^{\text{excess}} = x(1-x)\{w_{\text{A}}(1-x) + w_{\text{B}}x\}, \tag{A.1}$$

where w_{A} and w_{B} are the interaction parameters when a component of A enters a group of B, and when a component of B enters a group of A, respectively. These represent the slopes of the g^{excess} curve at the endpoints on the B side and A side, with a positive slope indicating that the system becomes energetically unstable after mixing, while a negative slope indicates that the system becomes energetically stable. The Gibbs energy curves for both the cases where w_{B} is positive or negative are shown in Fig. A.8.

For the asymmetric model, the first and second derivatives of the molar

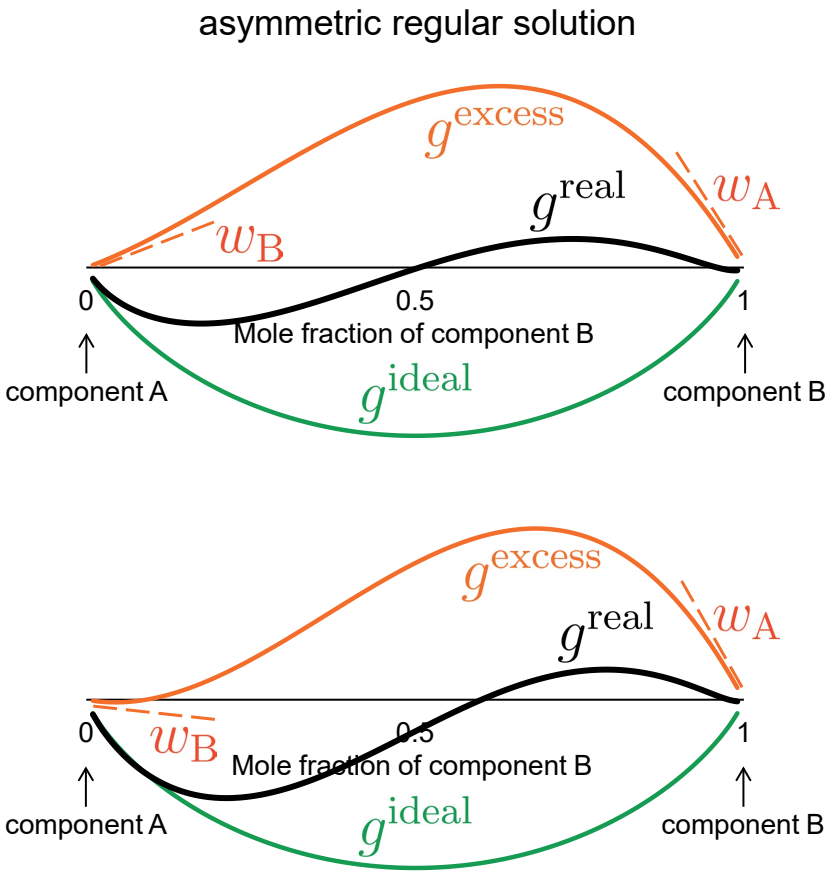

Figure A.8: Schematic diagrams of the molar Gibbs energy for asymmetric regular solutions of two components A and B. The green curve represents that of an ideal solution g^{ideal}, which is common to all regular solution models. The orange curve represents the molar excess Gibbs energy for a regular solution g^{excess}. The bold black curve represents the sum of these: the molar Gibbs energy of mixing g^{real}. The interaction parameters w_{A} and w_{B} are represented by the slopes of the g^{excess} curve at the endpoints on the B side and A side, respectively. In both the upper and lower panels, w_{A} is positive; w_{B} is positive in the upper panel and negative in the lower panel.

Gibbs energy of mixing g^{real} ($= g^{\mathrm{ideal}} + g^{\mathrm{excess}}$) with respect to x are given by:

$$\left(\frac{\partial g^{\mathrm{real}}}{\partial x}\right)_{T,P} = RT \ln\left(\frac{x}{1-x}\right) + w_{\mathrm{A}} x(2-3x) + w_{\mathrm{B}}(3x^2 - 4x + 1), \quad \text{(A.2)}$$

$$\left(\frac{\partial^2 g^{\mathrm{real}}}{\partial x^2}\right)_{T,P} = \frac{RT}{x(1-x)} + 2\{w_{\mathrm{A}}(1-3x) + w_{\mathrm{B}}(3x-2)\}. \quad \text{(A.3)}$$

In the asymmetric model, the signs of the slopes at both ends of g^{excess}, i.e., w_{A} and w_{B}, are important. When combining Eqs. (A.2) and (A.3), if both $w_{\mathrm{A}} > 0$ and $w_{\mathrm{B}} > 0$, the relationship between x_{bi} and x_{spi} at a given T or P will be a one-to-one correspondence, just like in the symmetric model. As is well known, the silicate–water system has a large miscibility gap (e.g., Paillat et al., 1992; Shen and Keppler, 1997; Bureau and Keppler, 1999), so $g^{\mathrm{excess}} > 0$ must hold over a wide range of x. Therefore, the assumption that both $w_{\mathrm{A}} > 0$ and $w_{\mathrm{B}} > 0$ seems reasonable.

However, this case may not strictly match the behavior of real systems. For example, on the silicate-rich side, when water dissolves, it is slightly exothermic (i.e., $g^{\mathrm{excess}} < 0$), as suggested by HF solution calorimetry of hydrous volcanic glasses synthesized at high temperature and pressure (Clemens and Navrotsky, 1987; Richet et al., 2004; 2006). If this experimental result is valid, the correct assumption would be $w_{\mathrm{A}} > 0$ and slightly $w_{\mathrm{B}} < 0$. In other words, the shape of the g^{excess} (and thus g^{real}) for hydrous magma is asymmetric, and its peak should be slightly shifted from $x = 0.5$ (Fig. A.9 (a)). But then again, in this case, the relationship between x_{bi} and x_{spi} at a given T or P becomes a complex multivalued function, as shown in Fig. A.9 (b). Specifically, this figure suggests that the spinodal curve corresponding to x_{bi} in the range $0 < x_{\mathrm{bi}} < 1/3$ intersects with the spinodal curve corresponding to x_{bi} in the range $2/3 < x_{\mathrm{bi}} < 1$, which is unrealistic.

Appendix A.2. Three-component asymmetric model

Thus, the theoretical equations for a two-component asymmetric regular solution do not fit the actual energy curves of g^{excess} (and g^{real}) well. This issue could be addressed by increasing the number of components distinguished, thereby increasing the number of unknown interaction parameters w. For example, in the case of a three-component asymmetric regular solution, the expression for g^{excess} can be written as follows (Kakuda

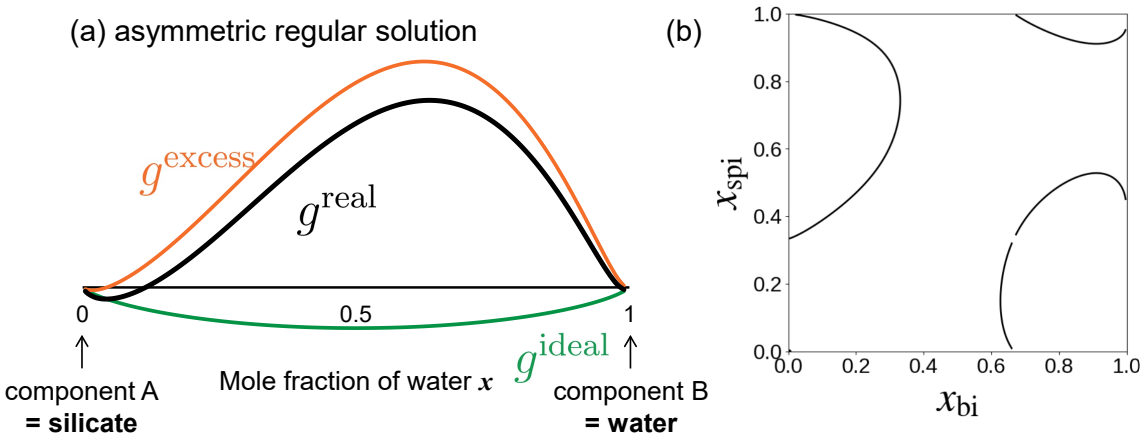

Figure A.9: (a) Schematic diagram of the molar Gibbs energy for a realistic hydrous magma, assuming it to be an asymmetric regular solution of anhydrous silicate (melt) and water (vapor). The meaning of each curve is the same as in Fig. A.8. Components A and B correspond to silicate and water, respectively. (b) The relationship between x_{bi} and x_{spi} in a two-component asymmetric regular solution model. An example is shown for the case where $T = 1,000°\text{C}$, $w_{\text{A}} = 345.7$ kJ/mol, and $w_{\text{B}} = -1.0$ kJ/mol.

et al., 1994):

$$\begin{aligned} g^{\text{excess}} &= x_{\text{A}}x_{\text{A}}x_{\text{B}}w_{\text{AAB}} \\ &+ x_{\text{A}}x_{\text{B}}x_{\text{B}}w_{\text{ABB}} \\ &+ x_{\text{B}}x_{\text{B}}x_{\text{C}}w_{\text{BBC}} \\ &+ x_{\text{B}}x_{\text{C}}x_{\text{C}}w_{\text{BCC}} \\ &+ x_{\text{C}}x_{\text{C}}x_{\text{A}}w_{\text{CCA}} \\ &+ x_{\text{C}}x_{\text{A}}x_{\text{A}}w_{\text{CAA}} \\ &+ 2x_{\text{A}}x_{\text{B}}x_{\text{C}}w_{\text{ABC}}, \end{aligned} \tag{A.4}$$

where w_{ijk} is the interaction parameter between components in a triplet consisting of three components. Nishiwaki (2023) distinguished between the molecular species of water (molecular water H_2O_m and hydroxyl groups $-$OH) and considered hydrous magma as a three-component system consisting of the bridging oxygen of anhydrous silicate and these water species. Additionally, he attempted to determine the values of the seven w_{ijk} parameters and the shapes of g^{excess} (and g^{real}) over a wide range of temperatures and pressures. However, this problem is highly challenging from a linear algebraic standpoint, and the values reported in Nishiwaki

(2023) are likely to be incorrect. We are currently working on resolving this issue. In the end, although we know that the shape of g^{excess} (and g^{real}) is complex, as shown in Fig. A.9 (a), for now, we have no choice but to compromise and approximate hydrous magma as a two-component symmetric regular solution consisting of silicate and water. Consequently, this approach is consistent with the scheme adopted by Allabar and Nowak (2018).

Acknowledgments

The author would like to thank Marcus Nowak for sharing numerous detailed and insightful comments on the experiments and results from their team, which significantly contributed to the improvement of the manuscript. The author is grateful to Yosuke Yoshimura for discussing spinodal decomposition in gas–liquid systems induced by pressure changes. The author also appreciates Atsushi Toramaru for his insightful comments on his newly developed models, which contributed to enhancing the content of this paper. Special thanks go to Takeshi Ikeda for many discussions on the fundamentals of the thermodynamics of silicate–water immiscibility. Participation in the reading circle for a glass science text with Shigeru Yamamoto inspired the author of this study. Shumpei Yoshimura provided the author with some methods for calculating the mole fraction of water in magma. The content of this paper was deepened through discussions with Hidemi Ishibashi and Takayuki Nakatani. The author also wishes to thank Kitajima, an okonomiyaki restaurant, for providing delicious meals that sustained the author during the preparation of this manuscript. The manuscript was significantly improved through MP, Mathieu Colombier, and two anonymous reviewers' peer review, as well as the generous handling by Editor Chiara Maria Petrone. This work was supported by JSPS KAKENHI Grant Number JP23K19069. The author would like to thank Editage (www.editage.jp) for English language editing.

References

Allabar, A., and Nowak, M., 2018. Message in a bottle: Spontaneous phase separation of hydrous Vesuvius melt even at low decompression rates. *Earth Planet. Sci. Lett.* **501**, 192–201. https://doi.org/10.1016/j.epsl.2018.08.047

Allabar, A., Dobson, K. J., Bauer, C. C., and Nowak, M., 2020a. Vesicle shrinkage in hydrous phonolitic melt during cooling. *Contrib. Mineral. Petrol.* **175** (3), 21. https://doi.org/10.1007/s00410-020-1658-3

Allabar, A., Salis Gross, E., and Nowak, M., 2020b. The effect of initial H_2O concentration on decompression-induced phase separation and degassing of hydrous phonolitic melt. *Contrib. Mineral. Petrol.* **175** (3), 22. https://doi.org/10.1007/s00410-020-1659-2

Aursand, P., Gjennestad, M. A., Aursand, E., Hammer, M., and Wilhelmsen, Ø., 2017. The spinodal of single- and multi-component fluids and its role in the development of modern equations of state. *Fluid Phase Equilib.* **436**, 98–112. https://doi.org/10.1016/j.fluid.2016.12.018

Bureau, H., and Keppler, H., 1999. Complete miscibility between silicate melts and hydrous fluids in the upper mantle: experimental evidence and geochemical implications. *Earth Planet. Sci. Lett.* **165** (2), 187–196. https://doi.org/10.1016/S0012-821X(98)00266-0

Burnham, C. W., and Jahns, R. H., 1962. A method for determining the solubility of water in silicate melts. *Am. J. Sci.* **260** (10), 721–745. https://doi.org/10.2475/ajs.260.10.721

Cahn, J. W., 1965. Phase separation by spinodal decomposition in isotropic systems. *J. Chem. Phys.* **42** (1), 93–99. https://doi.org/10.1063/1.1695731

Cahn, J. W., and Hilliard, J. E., 1959. Free energy of a nonuniform system. III. Nucleation in a two-component incompressible fluid. *J. Chem. Phys.* **31** (3), 688–699. https://doi.org/10.1063/1.1730447

Charlier, B., and Grove, T. L., 2012. Experiments on liquid immiscibility along tholeiitic liquid lines of descent. *Contrib. Mineral. Petrol.* **164**, 27–44. https://doi.org/10.1007/s00410-012-0723-y

Clemens, J. D., and Navrotsky, A., 1987. Mixing properties of $NaAlSi_3O_8$ melt–H_2O: new calorimetric data and some geological implications. *J. Geol.* **95** (2), 173–188. https://doi.org/10.1086/629118

Cluzel, N., Laporte, D., Provost, A., and Kannewischer, I., 2008. Kinetics of heterogeneous bubble nucleation in rhyolitic melts: implications for the number density of bubbles in volcanic conduits and for pumice textures. *Contrib. Mineral. Petrol.* **156** (6), 745–763. https://doi.org/10.1007/s00410-008-0313-1

Debenedetti, P. G., 2000. Phase separation by nucleation and by spinodal decomposition: Fundamentals. In: Kiran, E., Debenedetti, P. G., Peters, C. J. (Eds.), Supercritical Fluids. Nato Science Series **366**, 123–166.

https://doi.org/10.1007/978-94-011-3929-8_5

Gardner, J. E., Hilton, M., and Carroll, M. R., 1999. Experimental constraints on degassing of magma: isothermal bubble growth during continuous decompression from high pressure. *Earth Planet. Sci. Lett.* **168** (1–2), 201–218. https://doi.org/10.1016/S0012-821X(99)00051-5

Gardner, J. E., Wadsworth, F. B., Carley, T. L., Llewellin, E. W., Kusumaatmaja, H., and Sahagian, D., 2023. Bubble formation in magma. *Annu. Rev. Earth Planet. Sci.* **51**, 131–154. https://doi.org/10.1146/annurev-earth-031621-080308

Giachetti, T., Druitt, T. H., Burgisser, A., Arbaret, L., and Galven, C., 2010. Bubble nucleation, growth and coalescence during the 1997 Vulcanian explosions of Soufrière Hills Volcano, Montserrat. *J. Volcanol. Geotherm. Res.* **193** (3–4), 215–231. https://doi.org/10.1016/j.jvolgeores.2010.04.001

Gonnermann, H. M., and Gardner, J. E., 2013. Homogeneous bubble nucleation in rhyolitic melt: Experiments and nonclassical theory. *Geochem. Geophys. Geosyst.* **14** (11), 4758–4773. https://doi.org/10.1002/ggge.20281

Guggenheim, E. A., 1952. Mixtures: the theory of the equilibrium properties of some simple classes of mixtures solutions and alloys. Clarendon Press.

Haasen, P., 1996. Physical metallurgy. Cambridge University Press.

Hajimirza, S., Gonnermann, H. M., Gardner, J. E., and Giachetti, T., 2019. Predicting homogeneous bubble nucleation in rhyolite. *J. Geophys. Res. Solid Earth* **124** (3), 2395–2416. https://doi.org/10.1029/2018JB015891

Hajimirza, S., Gonnermann, H. M., and Gardner, J. E., 2021. Reconciling bubble nucleation in explosive eruptions with geospeedometers. *Nat. Commun.* **12** (1), 283. https://doi.org/10.1038/s41467-020-20541-1

Hajimirza, S., Gardner, J. E., and Gonnermann, H. M., 2022. Experimental demonstration of continuous bubble nucleation in rhyolite. *J. Volcanol. Geotherm. Res.* **421**, 107417. https://doi.org/10.1016/j.jvolgeores.2021.107417

Hamada, M., Laporte, D., Cluzel, N., Koga, K. T., and Kawamoto, T., 2010. Simulating bubble number density of rhyolitic pumices from Plinian eruptions: constraints from fast decompression experiments. *Bull. Volcanol.* **72** (6), 735–746. https://doi.org/10.1007/s00445-010-0353-z

Hamilton, D. L., Burnham, C. W., and Osborn, E. F., 1964. The

solubility of water and effects of oxygen fugacity and water content on crystallization in mafic magmas. *J. Petrol.* **5** (1), 21–39. https://doi.org/10.1093/petrology/5.1.21

Hirth, J. P., Pound, G. M., and St Pierre, G. R., 1970. Bubble nucleation. *Metall. Trans.* **1** (4), 939–945. https://doi.org/10.1007/BF02811776

Houghton, B. F., Carey, R. J., Cashman, K. V., Wilson, C. J., Hobden, B. J., and Hammer, J. E., 2010. Diverse patterns of ascent, degassing, and eruption of rhyolite magma during the 1.8 ka Taupo eruption, New Zealand: evidence from clast vesicularity. *J. Volcanol. Geotherm. Res.* **195** (1), 31–47. https://doi.org/10.1016/j.jvolgeores.2010.06.002

Hurwitz, S., and Navon, O., 1994. Bubble nucleation in rhyolitic melts: Experiments at high pressure, temperature, and water content. *Earth Planet. Sci. Lett.* **122** (3–4), 267–280. https://doi.org/10.1016/0012-821X(94)90001-9

Iacono-Marziano, G., Schmidt, B. C., and Dolfi, D., 2007. Equilibrium and disequilibrium degassing of a phonolitic melt (Vesuvius AD 79 "white pumice") simulated by decompression experiments. *J. Volcanol. Geotherm. Res.* **161** (3), 151–164. https://doi.org/10.1016/j.jvolgeores.2006.12.001

Kakuda, Y., Uchida, E., and Imai, N., 1994. A new model of the excess Gibbs energy of mixing for a regular solution. *Proc. Jpn. Acad. B* **70** (10), 163–168. https://doi.org/10.2183/pjab.70.163

Lavallée, Y., Dingwell, D. B., Johnson, J. B., Cimarelli, C., Hornby, A. J., Kendrick, J. E., von Aulock, F. W., Kennedy, B. M., Andrews, B. J., Wadsworth, F. B., Rhodes, E., and Chigna, G., 2015. Thermal vesiculation during volcanic eruptions. *Nature* **528** (7583), 544–547. https://doi.org/10.1038/nature16153

Le Gall, N., and Pichavant, M., 2016. Homogeneous bubble nucleation in H_2O- and H_2O–CO2- bearing basaltic melts: Results of high temperature decompression experiments. *J. Volcanol. Geotherm. Res.* **327**, 604–621. https://doi.org/10.1016/j.jvolgeores.2016.10.004

Liu, Y., Zhang, Y., and Behrens, H., 2005. Solubility of H_2O in rhyolitic melts at low pressures and a new empirical model for mixed H_2O-–CO_2 solubility in rhyolitic melts. *J. Volcanol. Geotherm. Res.* **143** (1–3), 219–235. https://doi.org/10.1016/j.jvolgeores.2004.09.019

Makhluf, A. R., Newton, R. C. and Manning, C. E., 2020. Experimental investigation of phase relations in the system $NaAlSi_3O_8$–H_2O at high temperatures and pressures: Liquidus relations, liquid-vapor mixing, and

critical phenomena at deep crust-upper mantle conditions. *Contrib. Mineral. Petrol.* **175** (8), 76. https://doi.org/10.1007/s00410-020-01711-2

Mangan, M., Mastin, L., and Sisson, T., 2004. Gas evolution in eruptive conduits: combining insights from high temperature and pressure decompression experiments with steady-state flow modeling. *J. Volcanol. Geotherm. Res.* **129** (1–3), 23–36. https://doi.org/10.1016/S0377-0273(03)00230-0

Marks, P. L., and Nowak, M., 2025a. Vesiculation dynamics—Part 1: Decompression-induced H_2O vesicle formation in the Lower Laacher See phonolitic melt. *Eur. J. Mineral.* **37** (4), 385–412. https://doi.org/10.5194/ejm-37-385-2025

Marks, P. L., and Nowak, M., 2025b. Vesiculation dynamics–Part 2: Decompression-induced H_2O vesicle growth, onset, and progression of coalescence. *Eur. J. Mineral.* **37** (4), 413–435. https://doi.org/10.5194/ejm-37-413-2025

Marxer, H., Bellucci, P., and Nowak, M., 2015. Degassing of H_2O in a phonolitic melt: A closer look at decompression experiments. *J. Volcanol. Geotherm. Res.* **297**, 109–124. https://doi.org/10.1016/j.jvolgeores.2014.11.017

Moore, G., Vennemann, T., and Carmichael, I. S. E., 1998. An empirical model for the solubility of H_2O in magmas to 3 kilobars. *Am. Mineral.* **83** (1–2), 36–42. https://doi.org/10.2138/am-1998-1-203

Nishiwaki, M., 2023. Chemical-thermodynamic explorations on the dissolution of water in magma: Breaking of the ideal mixing model and estimations of temperature change with decompression-induced vesiculation. Doctoral Dissertation, Kyushu University. https://catalog.lib.kyushu-u.ac.jp/opac_detail_md/?reqCode=frombib&lang=0&amode=MD823&opkey=B168673756684664&bibid=6787423&start=1&bbinfo_disp=0

Nishiwaki, M., and Toramaru, A., 2019. Inclusion of viscosity into classical homogeneous nucleation theory for water bubbles in silicate melts: Reexamination of bubble number density in ascending magmas. *J. Geophys. Res. Solid Earth* **124** (8), 8250–8266. https://doi.org/10.1029/2019JB017796

Paillat, O., Elphick, S. C., and Brown, W. L., 1992. The solubility of water in $NaAlSi_3O_8$ melts: a re-examination of Ab–H_2O phase relationships and critical behaviour at high pressures. *Contrib. Mineral. Petrol.* **112**, 490–500. https://doi.org/10.1007/BF00310780

Preuss, O., Marxer, H., Ulmer, S., Wolf, J., and Nowak, M., 2016. Degassing of hydrous trachytic Campi Flegrei and phonolitic Vesuvius melts: Experimental limitations and chances to study homogeneous bubble nucleation. *Am. Mineral.* **101** (4), 859–875. https://doi.org/10.2138/am-2016-5480

Richet, P., Hovis, G., and Whittington, A., 2006. Water and magmas: Thermal effects of exsolution. *Earth Planet. Sci. Lett.* **241** (3–4), 972–977. https://doi.org/10.1016/j.epsl.2005.10.015

Richet, P., Hovis, G., Whittington, A., and Roux, J., 2004. Energetics of water dissolution in trachyte glasses and liquids. *Geochim. Cosmochim. Acta* **68** (24), 5151–5158. https://doi.org/10.1016/j.gca.2004.05.050

Roedder, E., 1978. Silicate liquid immiscibility in magmas and in the system K_2O–FeO–Al_2O_3–SiO_2: an example of serendipity. *Geochim. Cosmochim. Acta* **42** (11), 1597–1617. https://doi.org/10.1016/0016-7037(78)90250-8

Sahagian, D., and Carley, T. L., 2020. Explosive volcanic eruptions and spinodal decomposition: A different approach to deciphering the tiny bubble paradox. *Geochem. Geophys. Geosyst.* **21** (6), e2019GC008898. https://doi.org/10.1029/2019GC008898

Shannon, R. D., 1976. Revised effective ionic radii and systematic studies of interatomic distances in halides and chalcogenides. *Acta Crystallogr. A: Found. Adv.* **32** (5), 751–767. https://doi.org/10.1107/S0567739476001551

Shea, T., 2017. Bubble nucleation in magmas: A dominantly heterogeneous process?. *J. Volcanol. Geotherm. Res.* **343**, 155–170. https://doi.org/10.1016/j.jvolgeores.2017.06.025

Shen, A. H., and Keppler, H., 1997. Direct observation of complete miscibility in the albite–H_2O system. Nature **385** (6618), 710–712. https://doi.org/10.1038/385710a0

Sowerby, J. R., and Keppler, H., 2002. The effect of fluorine, boron and excess sodium on the critical curve in the albite–H_2O system. *Contrib. Mineral. Petrol.* **143** (1), 32–37. https://doi.org/10.1007/s00410-001-0334-5

Sparks, R. S. J., 1978. The dynamics of bubble formation and growth in magmas: A review and analysis. *J. Volcanol. Geotherm. Res.* **3** (1–2), 1–37. https://doi.org/10.1016/0377-0273(78)90002-1

Stolper, E., 1982a. Water in silicate glasses: An infrared spectroscopic study. *Contrib. Mineral. Petrol.* **81** (1), 1–7. https://doi.org/10.1007/

BF00371154

Stolper, E., 1982b. The speciation of water in silicate melts. *Geochim. Cosmochim. Acta* **46** (12), 2609–2620. https://doi.org/10.1016/0016-7037(82)90381-7

Suhendro, I., Toramaru, A., Harijoko, A., and Wibowo, H. E., 2022. The origins of transparent and non-transparent white pumice: A case study of the 52 ka Maninjau caldera-forming eruption, Indonesia. *J. Volcanol. Geotherm. Res.* **431**, 107643. https://doi.org/10.1016/j.jvolgeores.2022.107643

Tanaka, H., 1994. Critical dynamics and phase-separation kinetics in dynamically asymmetric binary fluids: New dynamic universality class for polymer mixtures or dynamic crossover?. *J. Chem. Phys.* **100** (7), 5323–5337. https://doi.org/10.1063/1.467197

Thivet, S., Pereira, L., Menguy, N., Médard, É., Verdurme, P., Berthod, C., Troadec, D., Hess, K. U., Dingwell, D. B., and Komorowski, J. C., 2023. Metastable liquid immiscibility in the 2018–2021 Fani Maoré lavas as a mechanism for volcanic nanolite formation. *Commun. Earth Environ.* **4** (1), 483. https://doi.org/10.1038/s43247-023-01158-w

Toramaru, A., 1989. Vesiculation process and bubble size distributions in ascending magmas with constant velocities. *J. Geophys. Res. Solid Earth* **94** (B12), 17523–17542. https://doi.org/10.1029/JB094iB12p17523

Toramaru, A., 1995. Numerical study of nucleation and growth of bubbles in viscous magmas. *J. Geophys. Res. Solid Earth* **100** (B2), 1913–1931. https://doi.org/10.1029/94JB02775

Toramaru, A., 2006. BND (bubble number density) decompression rate meter for explosive volcanic eruptions. *J. Volcanol. Geotherm. Res.* **154** (3–4), 303–316. https://doi.org/10.1016/j.jvolgeores.2006.03.027

Toramaru, A., 2022. Vesiculation and crystallization of magma: Fundamentals of volcanic eruption process, conditions for magma vesiculation. Springer Singapore. https://doi.org/10.1007/978-981-16-4209-8

Toramaru, A., 2025. The theoretical basis for textural indices of eruption dynamics: review and new conceptual models. *Earth Planets Space* **77**, 27. https://doi.org/10.1186/s40623-025-02146-4

Verhoogen, J., 1951. Mechanism of ash formation. *Am. J. Sci.* **249**, 723–739.

Wang, Q. X., Zhou, D. Y., Li, W. C., and Ni, H. W., 2021. Spinodal decomposition of supercritical fluid forms melt network in a silicate–H_2O

system. *Geochem. Perspect. Lett.* **18**, 22–26. https://doi.org/10.7185/geochemlet.2119

Yamashita, S., 1999. Experimental study of the effect of temperature on water solubility in natural rhyolite melt to 100 MPa. *J. Petrol.* **40** (10), 1497–1507. https://doi.org/10.1093/petroj/40.10.1497

Zhang, Y., 1999. H_2O in rhyolitic glasses and melts: measurement, speciation, solubility, and diffusion. *Rev. Geophys.* **37** (4), 493–516. https://doi.org/10.1029/1999RG900012

CRediT authorship contribution statement

Mizuki Nishiwaki: Conceptualization, Methodology, Formal analysis, Investigation, Writing – Original Draft, Writing – Review & Editing, Visualization, Project administration, Funding acquisition.

Declaration of competing interest

The author declares that he has no known competing financial interests or personal relationships that could have appeared to influence the work reported in this paper.

Data availability

The author confirms that the data supporting the findings of this study are available within the article.